Novel enhancing materials for biosensor design: The case studies of erbium-, gadolinium- and strontium-doped $Ca_{10}(PO_4)_6(OH)_2$ hydroxyapatite

Viviana Scognamiglio [a], Valeria Nocerino [b], Bruno Miranda [b], Luca De Stefano [b], Emanuela Tempesta [c], Manuela Rossi [d], Francesco Baldassarre [e], Angela Altomare [e], Francesco Capitelli [a,*]

[a] Institute of Crystallography, National Research Council, Department of Chemical Sciences and Materials Technologies, Via Salaria Km 29.300, 00015 Monterotondo Scalo, Rome, Italy
[b] Institute of Applied Sciences and Intelligent Systems, National Research Council, Department of Physical Sciences and Technologies of Matter, Via Pietro Castellino 111, 80131 Naples, Italy
[c] Institute of Environmental Geology and Geoengineering, National Research Council, Department of Biology Agriculture and Food Sciences, Via Salaria Km 29.300, 00015 Monterotondo Scalo, Rome, Italy
[d] Department of Earth Sciences, Environment and Resources, University of Naples Federico II, Via Cintia 80126 Naples, Italy
[e] Institute of Crystallography, National Research Council, Department of Chemical Sciences and Materials Technologies, Via Amendola 122/o, 70126 Bari, Italy

ARTICLE INFO

ABSTRACT

Hydroxyapatite (HAp), ideal formula $Ca_{10}(PO_4)_6(OH)_2$, has unique physicochemical properties, including an excellent adsorption ability for functional biomolecules (e.g. nucleic acids, proteins) thanks to its specific large crystal surface. This property can be further improved with cationic and anionic replacements within the HAp framework. The adsorption of such biomolecules, indeed, can cause changes in the electric properties of the HAp surface in terms of resistivity and capacitance, generating the conditions for an improvement of the materials targeted for sensor applications. This work relates to the multiple routes for the synthesis of HAp materials, their electrochemical and structural investigations, and a short overview on the most well-known applications in sensor design. Moreover, with the aim of finding new promising HAp-based materials tailored for bioreceptor immobilization in biosensing, we underwent some doped-hydroxyapatite materials, specifically Sr-HAp, Gd-HAp, and Er-HAp, to a complete characterization. Electrochemical analyses, based on differential pulse voltammetry and cyclic voltammetry, evidenced improved analytical performances of HAp in terms of signal enhancement, repeatability, reproducibility, and reusability, in particular concerning the Er-HAp phase. A multi-methodological structural study, based on powder X-ray diffraction analysis, microscopy techniques (optical, electron, and fluorescence), energy dispersive X-ray spectroscopy (for chemical analyses), Fourier transform infrared spectroscopy, and absorption/fluorescence spectroscopies, showed the mechanism of doping replacement in HAp crystallographic sites, owing to the results of the Rietveld refinement from powder X-ray data, and a strong fluorescence for Sr-HAp.

1. Survey on hydroxyapatite

Sensing materials based on $Ca_{10}(PO_4)_6(OH)_2$ hydroxyapatite (HAp) have gained significant attention in recent years thanks to their unique combination of biocompatibility, tunable properties, and versatility in different sensing applications, due to the unique properties of this well-known material both appreciated as natural material and as its synthetic counterpart.

HAp is a calcium phosphate mineral belonging to the group of $Ca_{10}(PO_4)_6(OH, F, Cl)_2$ apatite minerals, largely retrieved as an accessory phase in many Earth rocks and meteorites [1], and as the most abundant phase in hard human tissues, on all bones and teeth [2,3]. Below are reported the most recurrent issues for natural HAp (Fig. 1), and the most common routes to obtain synthetic HAp (Table 1).

* Corresponding author.
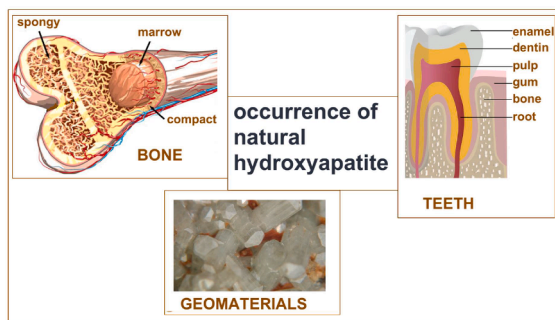*E-mail address:* francesco.capitelli@cnr.it (F. Capitelli).

Fig. 1. Occurrence of natural hydroxyapatite.

1.1. Occurrence of natural hydroxyapatite

In geological environments, HAp is commonly retrieved as secondary phase in igneous rocks like granite and pegmatite, usually as solid solution with the other two most known terms of apatite group, i.e. $Ca_{10}(PO_4)_6F_2$ fluorapatite and $Ca_{10}(PO_4)_6Cl_2$ chlorapatite; the apatite group belongs to a larger supergroup chemically constituted by phosphates, arsenates, vanadates, silicates, and sulphates [4][, related by the general formula $M1_4M2_6(TO_4)_6X_2$ [M = Ca^{2+}, Pb^{2+}, Ba^{2+}, Sr^{2+}, Mn^{2+}, Na^+, Ce^{3+}, La^{3+}, Y^{3+}, etc.; T = P^{5+}, As^{5+}, V^{5+}, Si^{4+}, S^{6+}, etc.; X = F^-, $(OH)^-$, Cl^-] [4].

HAp is also retrieved in phosphorite deposits, namely sedimentary rocks rich in phosphate minerals (P > 15–20 %) [5]. These deposits are important sources of raw phosphorus for fertilizer production, and HAp is a key component contributing to the phosphate content.

HAp is occasionally observed in some meteorites, providing insights into the distribution and the role of phosphorous in extraterrestrial sun system bodies [6,7].

1.2. Hydroxyapatite in human system

In vertebrate bones and teeth, HAp makes up the mineral fraction of hard tissues, providing them with the hardness and strength needed for structural support and protection. It is better indicated as biological hydroxyapatite, being on the geochemical point of view, a carbonated-HAp, with an exhaustive scientific production devoted to the distribution of $(CO_3)^{2-}$ within HAp framework [8-10].

In bones, HAp crystals provide structural support, being embedded within a collagen matrix, thus assuring at the same time rigidity and strength, conditions essential for weight-bearing and movement [11]. Besides, HAp acts as a reservoir for essential elements, on all calcium and phosphate, releasing them into the bloodstream as needed to maintain physiological balance [12]. Last, HAp is involved into the dynamic process of bone remodeling: in this case, osteoclasts break down HAp during bone resorption, while osteoblasts deposit new HAp during bone formation [13].

In teeth, HAp is the primary mineral component of tooth enamel, the hard outer layer of the teeth, also known to be the hardest substance in the human body [14], providing protection against wear and tear from chewing and exposure to acidic foods and beverages. Over the enamel, dentin also contains HAp, even if in a less densely packed form: this provides additional support and structure to the tooth, being slightly more flexible than enamel [15]. Last, in response to possible damage, teeth can undergo remineralization, where mineral substances lying in saliva provide calcium and phosphate useful to repair the HAp structure.

The investigation of natural HAp, both as geomaterial and from vertebrate biosystem, has led in the last decades to an enormous interest towards synthetic counterparts, largely employed as biomaterials in many technological applications, later briefly reviewed.

1.3. Routes of synthetic HAp

Methods for obtaining synthetic HAp can be classified as dry, wet, high-temperature, biogenic processes. Dry methods do not use a solvent, unlike wet methods. These methods grow particles of varying morphologies, phases and sizes [16]. Biogenic sources include the use of organic waste, eggshells, exoskeleton of marine organisms, bovine bones, fish scales and fish bones [17]. Each of these techniques has advantages and disadvantages, and leads to the synthesis of products with different chemical-physical characteristics, composition and properties. The choice of technique depends on the complexity and characteristics of the desired product, such as purity, size, crystallinity, morphology, and stoichiometry. Some techniques are scalable to the industrial level, while others are lab-scale; there are also combination methods in addition to the most popular reported in Table 1.

In brief:

In *dry synthesis* (mechanochemical, solid-state), the raw or reagent materials are taken in dry form and combined to synthesize HAp (without wet solvents). Mechanochemical synthesis exploits the processes of grinding and milling on the initial mixture of reagents in ball or planetary mills [18]. Through the combination of shear, compression and friction, high increases in local temperatures that contribute to the diffusion reaction, the transformation of the reactants into the desired products is induced [19-20]. It's possible to work in environmental conditions of temperature and pressure, high yields, possibility of producing smaller and more homogeneous particles than solid state synthesis (by high energy transfer mills), low cost. However, mechanochemical treatments have a disadvantage related to energy efficiency due to heat dissipation during the grinding process

Solid-state synthesis procedures [21] are generally run at high temperatures (900--1300 °C): a calculated amount of precursors (e.g. Ca and P salts for HAp synthesis) is used. The latter are finely ground, homogenized and compressed into pellets using a hydraulic press, in such a way as to bring the crystalline planes of the reactants closer together, promoting the ion diffusion process, induced by the high temperatures.

Table 1

Most popular methods for obtaining synthetic hydroxyapatite (LT: low temperature. HT: high temperature).

Method	Technique	Complexity/chemicals	Cost	Size	Crystallinity
Dry (LT)	Mechanochemical	low	low	variable	high
Dry (HT)	Solid-State	low	low	micron	very high
	Combustion	low	usually low	nano	variable
	Pyrolysis	medium	usually low	variable	high
Wet (LT)	Chemical-Precipitation	low	low	Variable	variable
	Hydrolysis	variable	high	Variable	variable
	Hydrothermal	medium-high	high	nano	high
	Sol-Gel	variable	variable	nano	variable
	Sono-chemical	low	low	nano	variable
	Emulsion	high	high	nano	low
Dry/Wet (LT/HT)	Biogenic Synth.*	low-medium	variable	variable	variable

* Biogenic synthesis: from bone waste-, marine animals exoskeleton-, and -eggshell sources.

Solid-state syntheses are characterized by low diffusion rate, and the presence of multiple phases in the final product. The density of the prepared sample is influenced by the palletization pressure, thus improving properties like Young's modulus, compressive strength, bending strength and tensile strength. Arkin et al. obtained high-purity HAp at a calcinating temperature of 1300 °C [22].

High Temperature Method (combustion, pyrolysis). In these methods, precursors are fully or partially burst at high temperatures. Formation of unnecessary CaP phases can be avoided in this process.

In combustion method, the reaction begins by heating the mixture of oxidizer and organic fuel in the aqueous phase, at a low temperature before a sudden rise in temperature. The final step in this process entails rapid cooling, which induces nucleation and prevents any further particle growth by producing nanopowders [23].

Pyrolysis, also called the gas-phase or aerosol method, is a chemical decomposition method of materials at high temperatures (above 430 °C) in the absence of oxygen, involving the spraying of a precursor substance in the hot zone of the electric furnace and particles can form from reactants in a gas generated by a liquid precursor [24,25]. It differs from combustion in that no fuel is mixed.

Wet methods (chemical precipitation, hydrolysis, hydrothermal, sol-gel, sono-chemical, emulsion). They refer to chemical synthesis in aqueous solutions containing the precursors of the reaction. Some of these methods are relatively simple and inexpensive.

Among the various wet processing methods, conventional chemical precipitation [23] is considered the simplest route for the synthesis of nano-sized HAp with regular morphology. For the preparation of pure HAp, a typical procedure involves the slow drop-by-drop addition of a calcium-based reagent to another reagent containing phosphate ions, under agitation, keeping the molar ratio of the Ca/P elements at 1.67 at pH>9, in accordance with the ideal stoichiometry of the HAp. Subsequently, the resulting precipitate, after a suitable maturation time, is washed several times to remove the reaction salts, filtered, dried in a stove and crushed into a powder [26]. Calcination (700 °C < T < 1000 °C) increases the crystallinity, if pure HAp is stable up to 900 °C without decomposition [27].

In hydrolysis method, HAp nanoparticles can be prepared by aqueous hydrolysis of other calcium phosphate (CaP) phases (anhydrous dicalcium phosphate, dicalcium dihydrate phosphate, tricalcium phosphate). During this process, the CaP phases dissolve in the water to form Ca^{2+} and $(PO_4)^{3-}$ ions, which subsequently react to precipitate in the form of HAp crystals [28,29].

The hydrothermal method is a chemical precipitation that takes place inside an autoclave and therefore the experimental conditions are at pressure at a temperature higher than the boiling point of water. The reaction between calcium and phosphate solution is triggered by high temperature and pressure, so it is a synthesis under pressure at temperatures >100°C and < 300°C [30].

The sol-gel method is a chemical procedure that uses colloidal particles or chemical solutions to generate a network of compounds (gels). It has been one of the first proposed methods for wet synthesis of HAp [31].

The sono-chemical methods are based on chemical reactions activated by powerful ultrasound, which generate acoustic cavitation in an aqueous phase. Nano-sized products are always produced [32,33].

The emulsion method is based on a isotropic micro dispersion, thermodynamically stabilized by the presence of surfactants, of two immiscible liquids (e.g. water and organic). The emulsion generates nano-sized particles with minimal agglomeration, and it depends on the type and concentration of surfactants used [34-36]

Biogenic synthesis method. It is possible to extract HAp from natural biogenic resources, such as shells and animal bones [17]. This possibility allows the recycling of some wastes; moreover, the presence of trace elements (Mg, Na, F, Sr) confers a high bioactivity of the HAp prepared from natural resources [37].

1.4. Structural properties of hydroxyapatite

Hydroxyapatite crystallizes in the hexagonal system, commonly in the centrosymmetric space group $P6_3/m$, unit cell parameters $a = b = 9.4302$ Å, $c = 6.8911$ Å [38], while monoclinic HAp crystallizes in centrosymmetric space group $P2_1/b$ with $a = 9.4214$ Å, $b = 2a$ Å, $c = 6.881$ Å, $\beta = 120°$ as unit cell parameters [38]. A comprehensive discussion on structural relationships among hexagonal and monoclinic HAp was presented by [39], suggesting that, although the differences between monoclinic and hexagonal HAp are very small (Fig. 2), they are enough to exert a substantial impact on some of their physicochemical properties, addressing the research also towards monoclinic HAp, due to their piezoelectric properties useful in some biomaterial application (they are mechanical–electrical transductors).

Hexagonal $P6_3/m$ HAp displays two calcium sites, engaged respectively in complex $Ca1O_9$ and $Ca2O_6(OH)$ coordinations. $Ca1O_9$ shows three bond distances repeated twice by symmetry, with values in the range 2.40 – 2.83 Å [40]. Usually the longer Ca1-O3 distance, slightly exceeds the bonding sphere of Ca, thus providing a weak contribution in terms of a bond valence calculation [41] for the Ca1 site: it is possible to deduce that, based on the refined distance values, the Ca1 site resembles a CaO_6 polyhedron, with the Ca1…O3 distances reviewed as weak interactions. $Ca2O_6(OH)$ resembles a distorted pentagonal bipyramid with five bonds (Ca2-O1, and two couples of symmetry-related Ca2-O3 bonds) on the equatorial plane, and vertices consisting of one O2 atom and one OH group [42].

The (OH) group in hexagonal $P6_3/m$ HAp lies on the $4e$ special position corresponding to a mirror plane, as observed in natural [1] and synthetic HAp [2]. In the monoclinic HAp structure, the (OH) groups lie on the screw 2_1 axes which run along the structure channels. Owing to the action of the glide plane, the (OH) groups point upward and downward in alternate nearest neighbor channels [38]. Phosphorous displays a regular tetrahedral coordination, common for all inorganic orthophosphates [43-45], with bond lengths in the range 1.55 –1.60 Å [46]. Carbonated-hydroxyapatite, so important in biological systems, display $(CO_3)^{2-}$ ions able to enter the HAp structure replacing OH, namely 'A type substitution', or replacing the phosphate ion, in this case namely 'B-type substitution' [9,35,38]. In some cases are observed mixed A-B substitutions [38].

The framework of hexagonal $P6_3/m$ HAp, whose crystal formula can also be reviewed as $[Ca1_4Ca2_6](PO_4)_6(OH)_2$, at its turn derived from general formula of apatite supergroup [4], can be interpreted as a three-dimensional network made up of columns of face-sharing $Ca1O_6$ metaprisms (a polyhedron intermediate between an octahedron and a trigonal prism), corner-connected to PO_4 tetrahedra down [001]. Such arrangement leads to the presence of one-dimensional tunnels occupied by $[Ca2_6(OH)_2]^{10+}$ counter-ions. The $Ca1O_6$ metaprism can be considered made by the six strongest Ca-O bond distances, not considering those over 2.8 Å. The HAp framework, often indicated as a zeolitic framework in analogy with that of those silicates [47], shows the ideal stoichiometry $[Ca1_4(PO_4)_6]^{10-}$, with the hexagonal channel containing $[Ca2_6(OH)_2]^{10+}$ moieties acting as counter-ions, while the Ca1-O3 interactions concur to stabilize the framework.

The monoclinic HAp shows almost complete structural similarity to the hexagonal HAp (Fig. 2), and the monoclinic cell setting has the c axis as the unique axis. The origin of the monoclinic cell is shifted toward (0, −1/2, 0) against the hexagonal cell and the b parameter is doubled. As a closing remark on the question of HAp symmetry, we quote the work of Pastero et al. [38], which states *either in nature (both in geological and bio-mineralized samples) or in laboratory grown hydroxyapatite crystals from pure aqueous solutions, allowing to say that the HAp hexagonality very often is nothing else but a manner of speaking. Moreover, the HAp platelets which grew elongated along the crystal channels, in the early stages of laboratory crystals and in mineralized biological tissues (tooth enamel, bones), are not due to the breaking of the hexagonal symmetry but to different growth rates of the different monoclinic pinacoids in zone with the crystal channels,*
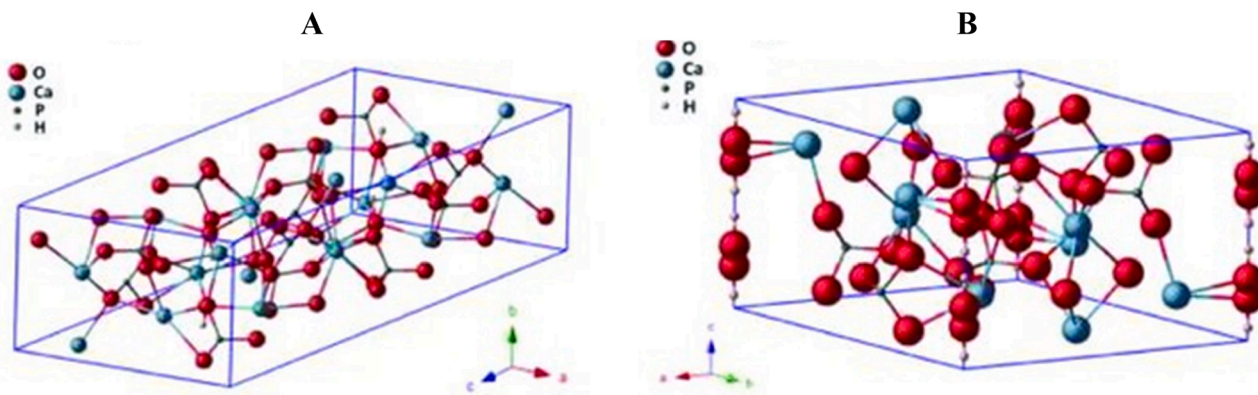
A   **B**

Fig. 2. Unit cells of monoclinic $P2_1/b$ (A) and hexagonal $P6_3/m$ (B) hydroxyapatite. Adapted from [39].

according to the varying supersaturation values experienced by the growth solution in a closed system [38].

1.5. Hydroxyapatite applications

Over the sensing applications later discussed, hydroxyapatite is widely recognized for its extensive applications in biomedicine due to its biocompatibility, osteoconductivity, and similarity to human bone minerals [48]. In orthopedics and dentistry, HAp is extensively used as a coating for metal implants, enhancing their integration with bone and promoting osteogenesis [49]. Its role in bone grafts and bone void fillers is crucial, aiding in the repair and regeneration of bone defects. Furthermore, HAp nanoparticles are being explored for drug delivery systems, particularly in targeting bone-related diseases, ensuring localized and sustained release of therapeutics [50]. In dentistry, HAp is employed in toothpaste and oral care products for its remineralizing properties, helping to repair enamel and reduce tooth sensitivity [51]. Beyond medical applications, hydroxyapatite finds use in environmental engineering, notably in water treatment processes for heavy metal ion adsorption [52], in cultural heritage as excellent layers against weathering for stony monuments [53], storage materials for nuclear wastes

[54], or luminesce materials for imaging [2]. The material versatility and bioactivity continue to drive research and development, expanding its applications in various fields, including tissue engineering, where HAp scaffolds support cell growth and tissue formation, promising advancements in regenerative medicine and beyond.

2. Hydroxyapatite as sensing material

Sensors are fundamental tools in various fields of daily life, from healthcare to environmental monitoring, offering real-time data to support decision-making. Hydroxyapatite has garnered considerable interest as a sensing material due to its remarkable biocompatibility, chemical stability, and tunable properties (Fig. 3).

2.1. Chemical physical properties of HAp

HAp-based sensing materials show several important properties that make them good candidates for sensor applications. As observed before in the Introduction, HAp is kwon for its biocompatibility, making it an excellent choice for biomedical applications. Its chemical composition closely resembles that of the human bone, reducing the possible risk of
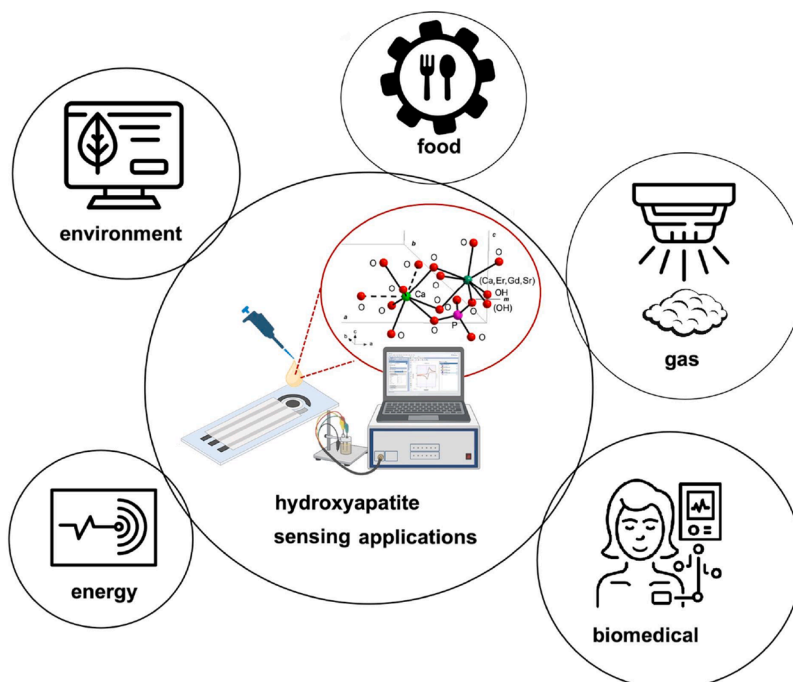

Fig. 3. Hydroxyapatite sensing applications.

rejection when used in medical applications (devices, implants) [42]. Additionally, HAp is chemically stable, resistant to degradation, and can withstand a wide range of pH values, which is crucial for applications in outdoor environments, such as wastewater monitoring [55]. The wide range of preparation of HAp allows researchers to finely adjust its composition, surface area, and crystallinity, in order to provide a material with good sensitivity and selectivity in sensing applications [40].

2.2. Environmental sensing

The excellent chemical stability of HAp makes it an ideal candidate for environmental sensing applications. It can be employed in the detection of various analytes, including heavy metals, pollutants, and ions in water and air [56]. Its resistance to chemical degradation ensures accurate and reliable data collection in harsh and challenging environmental conditions. The tunable surface area and composition of hydroxyapatite-based sensing materials allow for the selective and sensitive detection of specific contaminants, making them valuable tools for environmental monitoring and remediation [57].

2.3. Gas sensing

HAp-based sensing materials have shown promising gas sensing applications. They can detect gases such as ammonia, hydrogen, as well as volatile organic compounds [58]. These materials offer excellent sensitivity to changes in gas concentrations and can be improved to enhance selectivity and response time. Additionally, the porous structure of HAp promotes gas adsorption and desorption, providing rapid and reliable gas detection [59]. Such sensors find use in air quality monitoring applications.

2.4. Sensing in the food industry

The food industry benefits from HAp-based sensing materials in various ways. These materials can be utilized to detect contaminants, spoilage indicators, and pathogens in food products [60]. Their biocompatibility ensures that they can be incorporated into food packaging materials, offering real-time monitoring of food quality and safety. HAp sensors can also be used to monitor the freshness of perishable items, significantly supporting the screening of food chains and products [61].

2.5. Sensing in energy and electronics

HAp-based sensing materials have potential applications in the energy and electronics sectors [62]. They can be used in fuel cells and batteries for monitoring electrolyte conditions, contributing to improved performance and safety. Additionally, they are good humidity sensors [63] for electronic devices, providing accurate control of moisture levels to prevent damage and ensure long-term reliability.
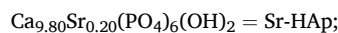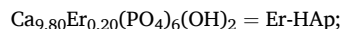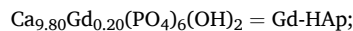
2.6. Sensing in biomedical applications

HAp-based sensing materials are used for various applications, including biosensors, drug delivery systems, and implantable sensors. HAp biocompatibility is crucial in the design of biosensors that can monitor physiological parameters, e.g. glucose levels, within the human body [64]. In addition, its porous structure can be used to load and release drugs in a controlled manner, enhancing patient treatment. Last, HAp coatings on medical implants, such as orthopedic and dental devices, improve their biocompatibility and integration with the surrounding tissues [65].

The following section of the work will be devoted to a case study of structural and electrochemical characterization of doped (Gd, Er, Sr) - and pure - HAp via the most reliable techniques for both the analyses.

3. Materials and methods

3.1. Synthesis

The hydroxyapatite samples investigated in the present study are labelled as:

$Ca_{9.80}Gd_{0.20}(PO_4)_6(OH)_2 = Gd\text{-}HAp;$

$Ca_{9.80}Er_{0.20}(PO_4)_6(OH)_2 = Er\text{-}HAp;$

$Ca_{9.80}Sr_{0.20}(PO_4)_6(OH)_2 = Sr\text{-}HAp;$

$Ca_{10.00}(PO_4)_6(OH)_2 = HAp\text{-}900.$

Er-HAp sample was prepared through solid-state synthesis: stoichiometric amounts of $CaCO_3$, $CaHPO_4$, and Er_2O_3 were manually ground and merged in an agate mortar for 1 h; the homogenized powder was then placed in alumina crucible and calcinated at high temperature (T = 1300 °C) for 7 h [22].

Gd-HAp sample was previously prepared through solid-state reaction, by mixing $CaCO_3$, $CaHPO_4$, and Gd_2O_3, pressing the resulting mixture up to form a pellet, and sintering it at 1300 °C in a furnace for 7 h [3].

Both Er- and Gd-HAp crystal formula, displaying rare earth (RE^{3+}) cations, should be expressed as $Ca_{9.80}RE_{0.20}(PO_4)_6(OH)_{2-x}O_x$ so that the charge balance generated by the RE^{3+} replacing Ca^{2+} is assured [2].

Sr-HAp sample was previously prepared via solid-state reaction too. A mixture of powders of $CaCO_3$, $CaHPO_4$ and $SrCO_3$ was pressed into pellets, sintered at 1250 °C for 12 h in a furnace [42].

Undoped HAp-900 sample, prepared to compare it with doped analogues, was previously obtained by chemical-precipitation at 25 °C by using $Ca(NO_3)_2$, $(NH_4)_2HPO_4$ and NaOH; successively, it was calcined at 900 °C for 2 h [2], according to [66].

3.2. Scanning electron microscopy/ energy dispersive X-ray spectroscopy

A Zeiss Merlin VP compact scanning electron microscopy (SEM) equipped with a charge compensation system and with Oxford Instruments Microanalysis EDS (Energy Dispersive X-ray Spectroscopy) X-max 50, was used for semi quantitative chemical analyses and morphological features of the samples. The Electron Microscope Field emission Zeiss Merlin VP Compact with camera Gemini II is composed by three secondary electron detectors SE2 (Classic Detector), VPSE (Variable Pressure) and InlensDuo (Low Voltage) and by two backscattered electron detectors AsB and InlensDuo. Chemical data processing and data imaging processing were achieved through dedicated software.

3.3. Granulometry investigation

Morphological investigations on HAp samples were achieved by using a Malvern Morphology G3-ID (Malvern Panalytical, Malvern, UK), an optical microscope fitted with a 500 mW Raman spectrometer (Kaiser Optics at 785 nm, Kaiser Optical Systems, Inc., Ann Arbor, MI, USA) with a 2 μm spot.

The optical microscope is suitable for the qualitative and quantitative analysis of particle size and particle shape in a range from 0.5 μm to several millimeters. In addition, an analyzer and polarizers can be manually integrated within the optical circuit. Scan mode is executed by using piezoelectric motors which assure the x–y–z movements with accuracy and repeatability of 1 μm. Particle size distribution analysis was achieved using the dedicated software Morphology G3 (User manual, issue 5, version MAN0410).

3.4. Powder X-ray diffraction

The Rigaku RINT2500 diffractometer, having a silicon strip Rigaku D/teX Ultra detector, was used to record powder X-ray diffraction (PXRD) data of Er-HAp sample data under the following experimental conditions: room temperature, 50 K, 200 mA, Debye–Scherrer geometry, monochromatic Cu Kα1 radiation (λ = 1.54056 Å) selected using an asymmetric Johansson Ge (111) crystal, step size of 0.02° (2θ), counting time of 4 s/step, 2θ angular range of 8–120° in transmission mode. Table 2 reports the main acquisition parameters of the Er-HAp sample. To reduce the possible effects of the preferred orientation of crystallites, a special glass capillary with a 0.5 mm internal diameter was filled with the sample and put in rotation on the axis of the goniometer. The software EXPO2013 [67] was employed in order to carry out all the steps of the structure solution process working in the reciprocal space: the determination of the unit cell parameters, via the specific N-TREOR09 software [68] and the space group, the solution using direct methods, and the Rietveld refinement. Qualitative investigation of the PXRD data was achieved through QUALX2.0 software using the POW_COD database [69] and the PDF-2 database [70]. Any other detail on Er-HAp crystal structure information (atomic positions, bonds, angles, etc.) and other indexed secondary phases (TCP, Er_2O_3, as discussed later) found in the pattern, may be retrieved from the joint CSD/ICSD (Cambridge Structural Database/Inorganic Crystal Structure Database) service [46], by quoting the deposit numbers CSD 2372033–2372035.

Structural investigations of other HAp samples reported in this paper: HAp-900 was previously described in [2]; Gd-HAp in [3], and Sr-HAp in [42].

3.5. Infrared spectroscopy

Fast Fourier Infrared (FTIR) spectra were recorded within the 525–4000 cm^{-1} frequency range with a resolution of 4 cm^{-1}, employing a Nicolet iS50 FT-IR Spectrometer instrument (Thermo Scientific). The instrument was equipped with an attenuated total reflectance (ATR) diamond crystal accessory for data acquisition. To acquire the FTIR spectra of all HAp samples, the powder was used without any prior treatment.

3.6. Electrochemical characterization

HAp electrochemical properties were evaluated by cyclic voltammetry (CV) and differential pulse voltammetry (DPV) using doped and undoped hydroxyapatites drop cast on graphite screen-printed electrodes (SPEs) [71]. These devices are three electrode systems containing an Ag reference electrode and graphite counter and working electrodes. 6 μL of a 1 mg/mL HAp dissolved in ethanol (H$_2$O: EtOH 2:1) were drop-cast onto the working electrode of the SPEs. The measurements were performed in a 100 μL-volume using a solution of 0.1 M KCl, 5 mM $K_3Fe(CN)_6/K_4Fe(CN)_6$ in a ratio 1:1 (v/v). The electrochemical analyses were carried out using a PalmSens4 [72].

3.7. Fluorescence spectroscopy and microscopy

HAp samples were dissolved in a mixture of distilled water and ethanol (H$_2$O: EtOH 2:1) to obtain a final concentration of 1 mg/mL. Absorption and fluorescence analyses were achieved using, respectively, a Jasco spectrophotometer V730 and a Jasco spectrofluorometer FP-8300, acquiring the absorption profiles in a wavelength window from 250 to 400 nm and fluorescence profiles in a wavelength window from 400 to 550 nm. Leica Z16 APO fluorescence microscope equipped with a camera Leica DFC300 was used for the fluorescence analysis of HAp samples drop cast on a silica-based support, using an excitation wavelength set at 365 nm.

4. Results and discussions

4.1. SEM-EDS

Detailed morphological analyses performed on Er-HAp and Gd-HAp microcrystalline powders revealed the presence materials occasionally porous, attributable to the existence of cavities of various sizes. The cavities show a diameter ranging from 0.5 to 7 μm in the Er-HAp sample (Fig. 4a), and from 0.5 μm to 4 μm in Gd-HAp (Fig. 4b). The fragment sizes vary significantly because of the morphology of the material. Smaller fragments exhibit irregular shapes, while larger ones occur with sub-rounded shapes. Fragment sizes can reach diameters up to 50 μm. The corresponding EDS analysis showed the presence of Ca, P, O and Er or Gd elements in the powders. No other elements were identified in the EDS spectra of both the powders (Table 3). The experimental crystal-chemical formulas are $(Ca_{4.76}Er_{0.19})_{4.95}(PO_4)_{3.05}(OH)_{1.01}$ (Er-HAp). and $(Ca_{4.76}Gd_{0.20})_{4.96}(PO_4)_{3.04}(OH)_{1.04}$ (Gd-HAp) in good agreement with nominal formulas.

The Sr-HAp sample is characterized by fragments of various sizes showing irregular morphology with accentuated edges and with porosity generally of reduced dimensions (Figs. 1d-4c). In the larger fragments, cavities can be observed in greater detail on the fractured surfaces (Fig. 4c). Most of the cavities are rounded with dimensions between 0.5 and 1.0 μm. Other cavities have elongated shapes, reaching up to 10 μm in length (Fig. 4d). The corresponding EDS analysis shows the presence of Ca, P, O and Sr elements in the powders. No other elements were identified in the EDS spectra of both the powders: compositionally, the experimental crystal formula in this case is $(Ca_{4.78}Sr_{0.19})_{4.97}(PO_4)_{3.03}(OH)_{1.02}$ (Table 1), in agreement with nominal formula.

In the HAp-900 sample, the microfragments of the powders show an irregular morphology with accentuated edges), with maximum lengths of 500 and 200 μm, respectively. The surfaces of the microfragments are not smooth, showing a framework made by different layers of nanoparticles (Fig. 4e). Besides, the particles visible on the surface of the fragments show faces, edges, and vertices attributable to crystals with irregular geometric shapes (Fig. 4f). In some cases, small cavities are also visible among the nanocrystals (Fig. 4f).

The analyses reveal a certain morphological difference between the samples rare earth -doped samples on one side, and Sr-doped and undoped HAp-900 on the other side. Specifically, the morphology of the samples containing RE elements aligns with data already present in the literature, which demonstrates the porosity and irregular and/or sub-spherical morphology of the powder fragments [3,73-74]. Similarly, for the Sr-HAp sample, we have found similarities with previous studies [75-78]. However, in our case, the fragments, besides being large and angular, also exhibit cavities, sometimes extensive ones. Last, concerning the undoped HAp-900 sample, the morphologies of the fragments and the nanocrystals align with those already documented in the

Table 2

Main acquisition and structure refinement parameters for the Er-HAp sample. FMLQ = Full Matrix Least Squares; Pearson VII [67].

Sample name	Er-HAp
Refined formula	$(Ca_{5.00}Er_{0.01})_2(PO_4)_6(OH)_2$
Formula weight	1007.80
Color	colorless
Temperature (K)	293
Wavelength (Å)	1.54056
2θ range (°); step (°)	10–120, 0.02
System, space group	Hexagonal, $P6_3/m$
$a = b$ (Å)	9.41266(8)
c (Å)	6.87806(12)
V (Å^3)	527.741(12)
Z; Density$_{calc.}$ (Mg·m^{-3})	1, 3.171
Refinement method	FMLQ
Bragg refl., parameters	1030, 78
R_p, R_{wp}, R_{exp} (%)	3.72, 5.73, 4.51
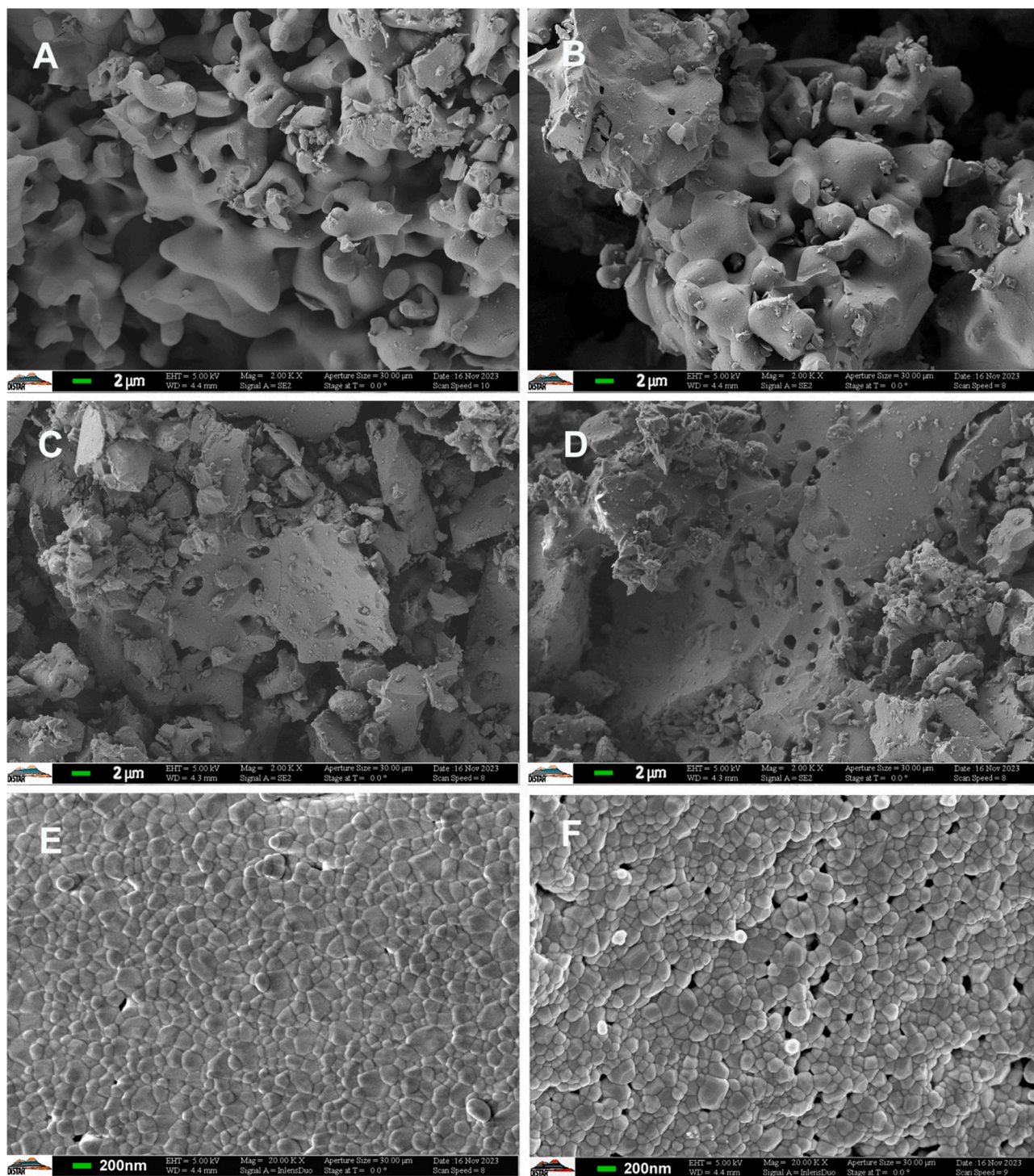
Fig. 4. A) Er-HAp sample: detail of the porous material characterized by the presence of rounded cavities of various sizes and smaller-sized fragments. B) Gd-HAp sample: detail of the porous material characterized by the presence of rounded cavities of various sizes and smaller-sized fragments. C) Sr-HAp sample: occurrence of fragments with different sizes; evidence of fracture surfaces of the cavities. D) Sr-HAp sample: cavities of various sizes and shapes present on the fresh fracture surfaces. E) HAp-900: high-magnification image of the compact surface of a powder fragment, made by nanocrystals. F) HAp-900. The image displays the shapes of the nanocrystals, where faces, edges, and vertices of crystals with irregular geometric shapes can be observed. Additionally, the cavities of various sizes and shapes occurring between the nanoparticles can be better observed (HAp-900 sample).

literature [78-82]. However, we observed smaller sizes in comparison with those reported in literature, and for the HAp-900 sample, the presence of shapes ascribable to geometric solids was not previously reported.
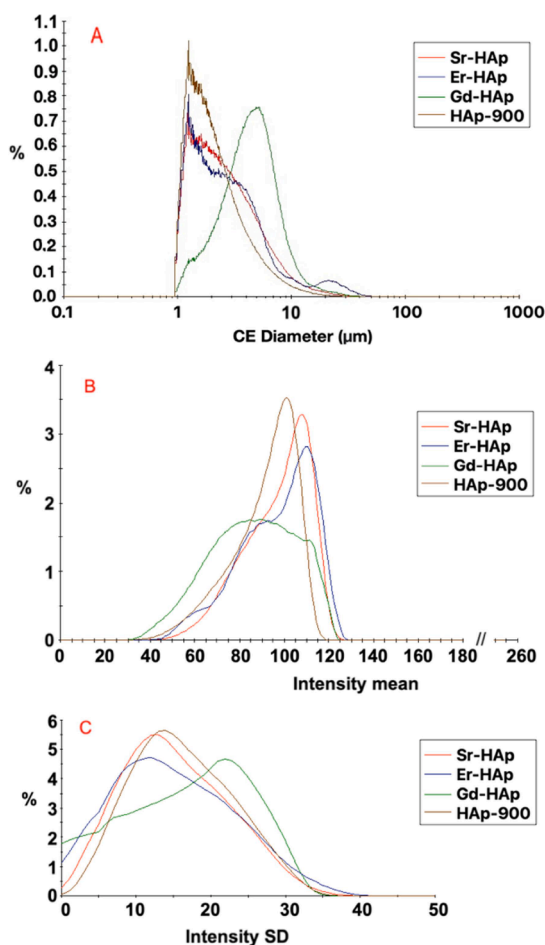
4.2. Analysis of granulometry

A particle size distribution analysis was performed, owing to the method of 'scanning optical microscopy' [83], based on the scanning of a large number of particles randomly disposed on a mount transparent to visible light. Particles are first photographed, after which the dedicated

Table 3
EDS semi-quantitative analysis of doped HAp samples under study.

Sample	Er-HAp	Gd-HAp	Sr-HAp
CaO	50.57(5)	50.61(27)	52.47(61)
SrO	–	–	3.80(24)
P_2O_5	40.86(42)	40.77(41)	41.94(48)
Gd_2O_3	–	6.84(14)	–
Er_2O_3	6.84(36)	–	–
F	–	–	–
Cl	–	–	–
$H_2O^{+\cdot*}$	1.73(2)	1.77(4)	1.80(1)
Tot.	*100.00*	*100.00*	*100.00*
8 CAT			
Ca	4.76(1)	4.76(2)	4.78(5)
Sr	–	0.00	0.19(1)
P	3.05(2)	3.04(2)	3.03(4)
Gd	–	0.20(0)	–
Er	0.19(1)	–	–
F	–	–	–
Cl	–	–	–
OH	1.01(1)	1.04(3)	1.02(1)
X	*1.01(1)*	*1.04(3)*	*1.02(1)*
Z	*3.05(2)*	*3.04(3)*	*3.03(4)*
M	*4.95(2)*	*4.96(3)*	*4.97(4)*

[*] Values calculated by scaling the analysis to 100. The average is calculated over 25 analysis points, with the standard deviation provided in parentheses.

Fig. 5. Analysis of granulometry of present HAp samples. A) Circle equivalent (CE) diameter distributions; B) Intensity mean distributions; C) Variance of the standard deviation of the intensity mean.

software Morphologi G3 measures the dimensions of each particle [83].

In Fig. 5 is possible to appreciate the trend of particle distributions of the doped HAp sample in comparison with undoped HAp-900. Analysis of the circle equivalent (CE) diameter, i.e. the normalization of particle dimensions to a sphere, allows observing that the granulometry increases for RE-doped HAp samples, especially for Gd-HAp peaking the limit of 5 μm, while Sr-HAp and undoped HAp-900 show very fine powders, about 1 μm (Fig. 5A). Another interesting parameter correlated with CE diameter is the intensity of transmitted light (Fig. 5B), which usually depends on several parameters, e.g. the particle size, the wavelength of the radiation, the refractive index of the particles and of the surrounding media, the shape of the particles, adsorption properties of the particles, their concentration, the thickness, and chemical content. These factors collectively influence the light behavior, influencing the intensity of transmitted light.

Besides, in Fig. 5C are reported the distributions of the standard deviations of the intensity of transmitted light. Some practical considerations arise from the observation of this distribution. Some of the previously reported parameters for intensity mean are fixed, such as light wavelength, refractive index of the surrounding medium, the shape and the concentration of the particles. Vice versa, the parameters that can affect the Intensity mean are the refractive index of the particles, the light absorption properties of the particles, and their thickness.

The refractive index of hydroxyapatite peaks low values, 1.65 for nw e 1.644 for ne. Such values depend on the composition, e.g. the calcium deficiency in comparison with the ideal formula $Ca_{10}(PO_4)(OH)_2$. Recent studies demonstrated that the pure calcium apatite is transparent to the visible light and to UV, while the divalent dopants replacing Ca make up defects at energies pertinent to the conduction band and the valence band, i.e. between 4.5 and 5.4 eV: europium doping increases of 20 % the transmittance of hydroxyapatite [84].

The increase of the transmittance stands for the increase of the transmitted light, and it is what is observable in HAp sample containing gadolinium, that, in periodic table, is just located as first neighbor of europium, while erbium, as also the strontium, caused the opposite effect. The reason of such discrepancy is, conceivably, the occurrence of a combined effect between several factors, which causes a general lowering of the transmittance in Er-HAp and Sr-HAp powders.

4.3. X-ray diffraction

About the Er-HAp sample here investigated, the crystal structure solution steps, from indexing to the structure model refinement, were achieved through the EXPO2013 software [67]. The indexation of the powder diffraction pattern, obtained by N-TREOR09 software [68] included in EXPO2013, revealed the hexagonal unit cell recurrent in HAp. Crystallite size, corresponding to a value of 137 nm, was estimated by the experimental pattern observing the diffraction peak at $2\theta = 25.86°$ using the Scherrer equation. The crystallinity value, 91 %, was obtained according to [85]: it is in good agreement with HAp values obtained by high-temperature synthesis [2,3,40], differently from HAp obtained at room temperature, as reported in [2,86].

A careful inspection of the PXRD pattern of Er-HAp sample, through QUALX2.0 package [69], highlighted well-defined sharp peaks of the HAp phase (JCPDS, PDF-2, 00–089–6437), with some unindexed diffraction peaks corresponding to $Ca_3(PO_4)_2$ tricalcium phosphate phase (β-TCP) (JCPDS, PDF-2, 00–070–2065) (Fig. 6, inset). The partial dissociation of HAp into TCP at temperatures higher than 900 °C was previously reported in literature [3,87]. Additionally, non-negligible amount of Er_2O_3 secondary phase was observed too (JCPDS, PDF-2, 00–077–0777), as well as traces of $CaCO_3$ (JCPDS, PDF-2, 00–047–1743) (Fig. 6, inset): both these phases are unreacted starting materials. A semi-quantitative estimation of mineralogical phases within the Er-HAp sample using the Rietveld method in EXPO2013 revealed Er-HAp for 81.4 %, β-TCP for 17.2 %, and Er_2O_3 for 0.6 %. Diffraction peaks corresponding to HAp, β-TCP and Er_2O_3 phases ere
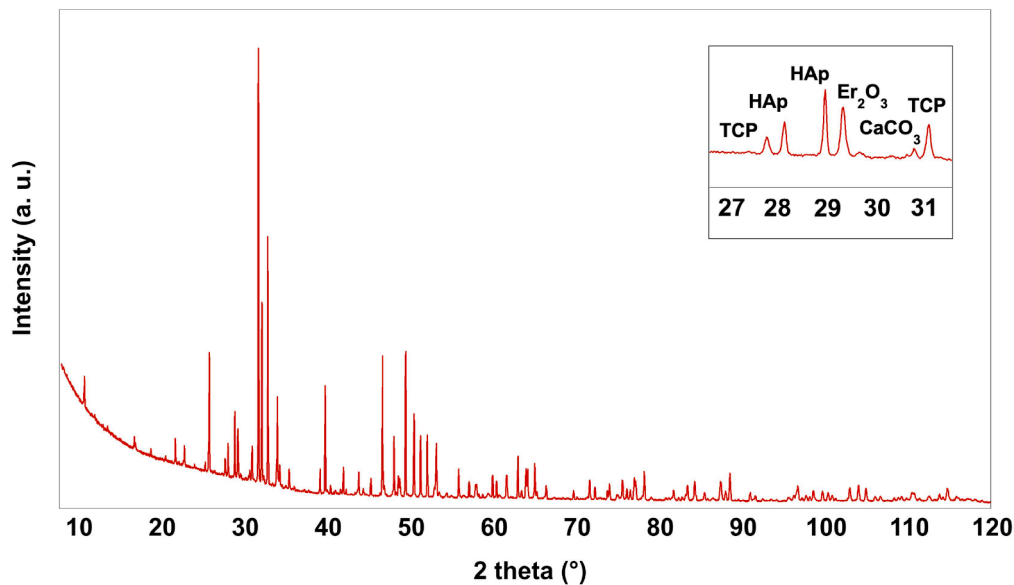
Fig. 6. Observed PXRD profile of the Er-HAp sample, compared with the reference HAp (JCPDS, PDF-2, 00–089–6438) peaks. Inset: secondary phases observed: (β-) TCP (JCPDS, PDF-2, 00–070–2065); Er_2O_3 (JCPDS, PDF-2, 00–077–0777); $CaCO_3$ (JCPDS, PDF-2, 00–047–1743).

depicted in the observed PXRD pattern of Er-HAp reported in Fig. 6.

The next step of the structure investigation revealed the hexagonal $P6_3/m$ space group for the HAp, while the structure solution was obtained via the direct methods procedure in EXPO2013, confirming the hexagonal $P6_3/m$ model reported in literature [ICSD, 2018]. The obtained structure was submitted to structural refinement by the Rietveld method, assuming both calcium sites as possible localizations of the dopant species (erbium). A simple refinement strategy was applied: in the site shared by Ca and Er, the positions and the thermal parameters of both occupants were constrained to be equal. Last, the sum of Ca and Er occupancies was fixed to 1.000: the Rietveld refinement was able to indicate the presence of Er in the site shared with Ca2, with a small site occupation factor (s.o.f.): the profile discrepancy factors increased when Er was excluded from Ca2 and Ca1 sites or included in Ca1. Final values of site occupancy for Ca2 and Er1 were 0.996(1)/0.004(1). Hydrogen atom was geometrically located by EXPO2013 software, at a fixed distance (0.96 Å) from O4 parent oxygen atom. Table 4 reports atomic positions and isotropic atomic displacement parameters.

For what concern a structural description of the Er-HAp sample, the structure is characterized by two cationic sites filled by calcium, and one anionic site with a phosphorous atom. Three oxygen atoms and one hydroxyl group (Table 4). All the atoms are placed on sites with s.o.f. = 1.00, with the exception of OH group (specifically O4 and H atoms) lying in special position corresponding to a mirror plan (s.o.f. = 0.5) [1]. Phosphorous makes up the typical (PO_4) tetrahedral group of ortho-phosphates, in which the P-O bond distances (Table 5) are aligned with those retrieved in other HAp structure descriptions from powder X-ray diffraction [88-89], i.e. with P-O values a bit longer than analogues

Table 4
Atomic positions, and isotropic displacement parameters in Er-HAp structure.

atom	x	y	z	Ueq
Ca1	2/3	1/3	1.0004(6)	0.0050
Ca2	0.2523(3)	0.2458(3)	3/4	0.0050
Er1	0.2523	0.2458	3/4	0.0050(4)
P	0.3988(4)	0.3682(3)	1/4	0.0048(7)
O1	0.3214(8)	0.4857(8)	1/4	0.0189(10)
O2	0.5952(8)	0.4667(9)	1/4	0.0189
O3	0.3375(6)	0.2482(6)	1.0671(6)	0.0189
O4$_{OH}$	0	0	0.7027(19)	0.0189
H	0	0	0.5636	0.0226

Table 5
Bond distances (Å) and bond valence parameters (bvp) in Er-HAp sample.

Bond		distance	bvp
Ca1-O	=	3 × 2.385(5)	*3 × 0.323*
Ca1-O2	=	3 × 2.412(7)	*3 × 0.300*
Ca1-O3	=	3 × 2.823(5)	*3 × 0.099*
Ca2-O1	=	2.665(9)	*0.152*
Ca2-O2	=	2.345(7)	*0.360*
Ca2-O3	=	2 × 2.320(5)	*2 × 0.385*
Ca2-O3	=	2 × 2.450(7)	*2 × 0.271*
Ca2-O4	=	2.367(3)	*0.169*
P-O1	=	1.600(7)	*1.047*
P-O2	=	1.601(7)	*1.044*
P-O3	=	2 × 1.594(5)	*2 × 1.065*

retrieved in single-crystal XRD refinements [46].

The Ca atoms are engaged in complex co-ordinations: Ca1 in a CaO_9 polyhedron (Fig. 7), with three couples of bond distances related by symmetry, ranging from 2.385(5)–2.823(5) Å. The Ca1-O3 distance slightly exceeds the bonding sphere of Ca, providing a weak contribution to the bond valence [41] to Ca1 (Table 5), thus suggesting the environment of the Ca1 site as a CaO_6 polyhedron surrounded by three Ca1…O3 weak interactions related per symmetry. Ca1-O distances are meanly a bit shorter compared with analogous distances in HAp
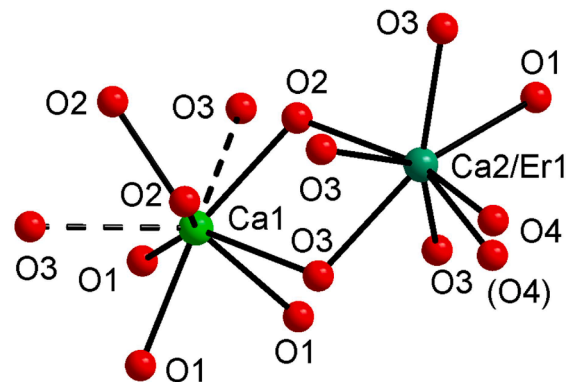
Fig. 7. Environment of Ca1 and Ca2/Er1 structural sites in hydroxyapatite. Dashed lines: Ca-O interactions > 2.8 Å O4 = (OH) site.

structures [46]. The Ca2 polyhedron displays a CaO$_6$(OH) coordination, resembling a distorted pentagonal bipyramid with five bonds (Ca2-O1 and two couples of symmetry-related Ca2-O3 bonds) on the equatorial plane, and vertices consisting of one O2 atom and one OH group. The Ca2-O distances are in the range 2.320(5)–2.665(9) Å (Table 5). Analysis of bond valence parameters [41], showed respectively for Ca1, Ca2 and P sites the values of 2.17, 1.99 and 4.22 valence units, suggesting a weak underbonding at the Ca1 site, and a general overbonding in P-O distances, as discussed before and observed in Table 5.

The three-dimensional framework of Er-HAp reflects what previously stated in the Introduction paragraph, with the presence of columns of face-sharing Ca1O$_6$ metaprisms (a polyhedron intermediate between an octahedron and a trigonal prism, corner-connected to PO$_4$ tetrahedra down [001]: such arrangement leads to the presence of one-dimensional tunnels occupied by [Ca2$_6$(OH)$_2$]$^{10+}$ counter-ions (Fig. 8). The HAp framework, shows ideal stoichiometry [Ca1$_4$(PO$_4$)$_6$]$^{10-}$, with the hexagonal channel containing [Ca2$_6$(OH)$_2$]$^{10+}$ moieties acting as counter-ions, while the Ca1-O3 interactions concur to stabilize the framework.

4.4. FTIR spectroscopy

FTIR spectroscopic investigations of HAp samples have been explored in various preliminary studies [2,3,40,90-92]. The vibrational characteristics of orthophosphate phases provide a unique molecular signature to FTIR spectra, predominantly highlighting the internal (PO$_4$)$^{3-}$ vibrational modes. The analysis of the IR spectrum of undoped hydroxyapatite (HAp-900), starts with the sharp peak at 3572 cm^{-1}, attributed to the stretching mode of the (OH)$^-$ group. This peak is the distinctive marker for identifying the HAp phase in FTIR spectra. This peak noticeably decreases within the three doped HAp samples of Er, Gd, and Sr (Fig. 9, inset). In literature, in the case of Sr doping at various ratios, a decrease in the intensity of this (OH) peak is observed with increasing Sr concentration, as a result of the partial Sr^{2+} substitution for the Ca^{2+} ions surrounding the (OH) group [42,93].

In the lower wavenumber region (Fig. 9), the prominent peaks in the 1090–1000 cm^{-1} range are linked to the triply degenerated antisymmetric stretching modes (v_3) of the phosphate group (PO$_4$)$^{3-}$. A clearly observable peak at 960 cm^{-1} corresponds to the symmetric stretching of this anion. An intense peak at 627 cm^{-1} is attributed to the bending mode of the (OH)$^-$ group [2], and, analogously to the stretching mode peak observed at 3572 cm^{-1}, in literature for samples with different Sr% ratio, we observe a decrease in the intensity of this peak, imputable to
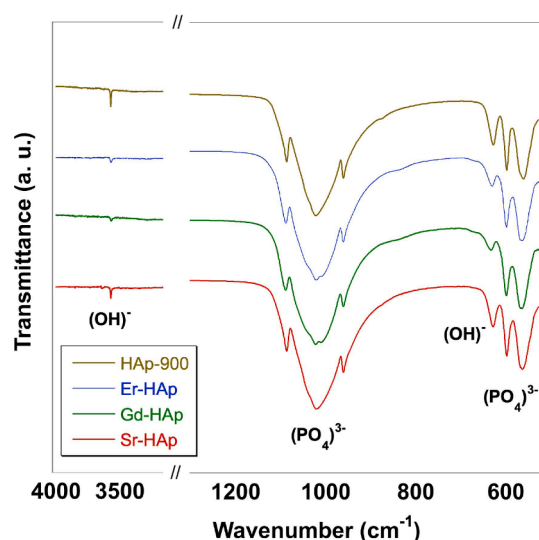

Fig. 9. FTIR spectra of undoped (HAp-900) and doped (Er-HAp, Gd-HAp and Sr-HAp) HAp samples, in the full range 4000–500 cm^{-1}.

the same substitution of Sr-Ca [93] previously observed. Last, two strong and sharp peaks at 597 and 560 cm^{-1} are attributed to the triple degenerate antisymmetric bending mode of the [PO$_4$]$^{3-}$ group [2]. An experimental correlation among the sharpness of the latter three peaks, 627, 597 and 560 cm^{-1}, with the crystallinity of the HAp samples, was reported in [94], matching in the present study the results for crystallinity from XRD analysis. A couple of medium-intensity and sharply defined peaks at 602 and 564 cm^{-1} are associated with the triple degenerate antisymmetric bending mode of the (PO$_4$)$^{3-}$ group [40]. Deuterated samples analysis reveals that the relatively sharp peak at 663 cm^{-1} is attributed to the O—H libration.

Compared to pure HAp sample, the doped HAp samples highlight some very weak shift position (Table 6), and a general loss of intensity of (OH) peaks at 3573 cm^{-1} (Fig. 9).

4.5. Electrochemical characterization

According to [40], 1 mg/ml of doped and undoped hydroxyapatites were solved in 50 % ethanol and sonicated with a Hielscher UP200St-Ultrasonic Transducer (200 W, 26 kHz, 30 min) (Hielscher
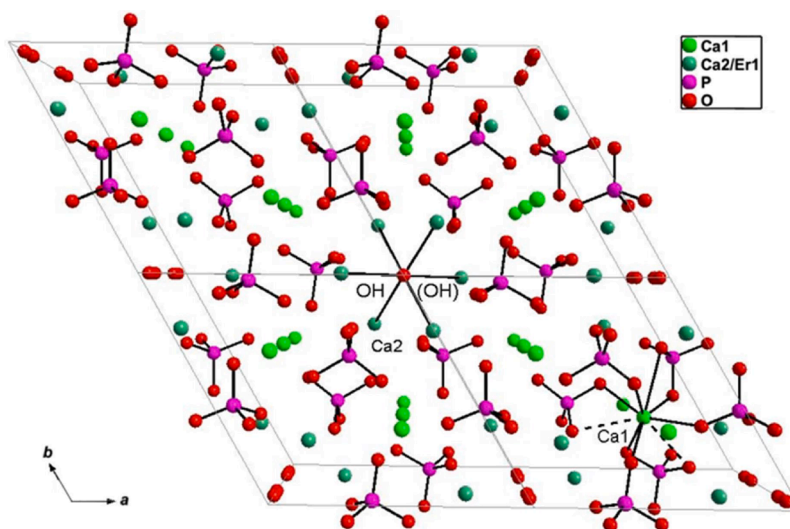

Fig. 8. Representation of the framework of Er-HAp: details of Ca1O$_6$ metaprisms, and Ca2$_6$(OH)$_2$ groups. (OH) groups correspond to O4 atoms. Ca1-O3 bonds over 2.8 Å are dashed for clarity. H atoms not drawn for clarity.

Table 6
FTIR band positions (wavenumbers, cm^{-1}) and relative assignments for HAp samples.

HAp-900	Er-HAp	Gd-HAp	Sr-HAp	Assignment
3573	3573	3572	3573	$\nu_s(OH)$
1090	1090	1090	1090	
1023	1023	1023	1023	$\nu_3(PO_4)^{3-}$
966	966	966	967	$\nu_1(PO_4)^{3-}$
630	633	636	630	$\delta(OH)$
603	603	600	603	
563	563	566	563	$\nu_4(PO_4)^{3-}$

Ultrasonics, Teltow, Germany). The obtained suspensions were drop cast on the working electrode of the SPEs and let dry at room temperature, dropping 2 μL in 3 times reaching a total volume of 6 μL. SPEs were previously treated by chronoamperometry (1.7 V, 180 s) in 0.1 M KCl, 0.05 M phosphate buffer pH 7 and rinsed with deionized water to remove salt residues. Then, CV and DPV analyses were conducted on

Fig. 10. Electrochemical characterization of bare SPE (black/dash curves) and SPE modified with undoped HAp-900, and Er-, Gd- and Sr-doped HAp by CV (A) and DVP (B) using 0.1 M KCl, 5 mM K$_3$Fe(CN)$_6$/K$_4$Fe(CN)$_6$ as electrochemical mediator.

bare SPE and SPEs modified with undoped and doped hydroxyapatites, using a solution of 0.1 M KCl, 5 mM K$_3$Fe(CN)$_6$/K$_4$Fe(CN)$_6$ in a ratio 1:1 (v/v) as electrochemical mediator. As reported in Fig. 10, both CV and DPV highlight a higher conductivity of Er-doped HAp in comparison with the other hydroxyapatites. Indeed, CV analyses show as the insertion of the erbium into the hydroxyapatite structure led to an improvement of the electrochemical performance in terms of peak intensity and peak-to-peak separation (Fig. 10A). At the same strength, DPV shows that the Er-doped HAp has a higher peak intensity (Fig. 10B).

4.6. Fluorescence spectroscopy

The analysis of the fluorescence revealed significant emission bands for both undoped and doped HAp samples. In Fig. 11, absorption and fluorescence spectra were reported to highlight the maximum excitation and emission peaks of each sample. Specifically, the signal acquisition window was set from 250 nm to 400 nm for the absorption spectrum and from 400 nm to 550 nm for the emission spectrum. The data show that a higher fluorescence intensity can be observed for Er-HAp (Fig. 11B) and further higher for Sr-HAp (Fig. 11D), compared to the undoped HAp (Fig. 11A) and to Gd-HAp (Fig. 11C), due to the presence of erbium and strontium (with this last as best). The same results were observed through fluorescence microscopy analysis with an excitation wavelength set at 365 nm.

5. Conclusions

This work relates to the possible application of hydroxyapatite in sensing applications. We have reviewed the most recurrent issues for natural HAp, those from both geological sources and biogenic sources in humans and vertebrates. We have successively described the most common routes for obtaining synthetic hydroxyapatite, including precipitation, sol-gel, hydrothermal, and spray drying techniques, etc.

Each method offers a unique set of advantages, enabling tailored properties suitable for specific sensing applications. Precipitation methods, for example, are cost-effective and easily scalable, making them suitable for large-scale production. Sol-gel synthesis, on the other hand, provides precise control over composition and morphology, allowing for fine-tuning of the material properties. Hydrothermal synthesis is ideal for producing hydroxyapatite with high crystallinity and purity, while spray drying enables the creation of nanoparticles and nanocomposites. By selecting the appropriate synthesis method, researchers can tailor hydroxyapatite-based sensing materials to meet the requirements of their specific applications.

The physicochemical properties of HAp were also reported, including the structural description of the most recurrent crystalline settings, i.e. those hexagonal and monoclinic.

The applications of HAp were disserted, focusing on those pertinent the sensors science, in particular in biomedical applications, environment, gas detection, food industry, energy and electronics.

Last, a case study of structural and electrochemical characterization of some doped and undoped HAp materials was presented. Rare earth (Gd; Er) - HAp and Sr - HAp were compared with pristine hydroxyapatite obtained with high temperature methods. These samples were comprehensively characterized by powder X-ray diffraction study, microscopy techniques (optical, electron, and fluorescence), EDS, FTIR, and absorption/fluorescence spectroscopies. The results showed the mechanism of doping replacement in HAp crystallographic sites, owing to the results of Rietveld refinement from powder X-ray diffraction data, and a higher fluorescence for Sr-HAp. Last, electrochemical investigations, based on differential pulse voltammetry and cyclic voltammetry, highlighted higher conductivity of Er-HAp in comparison with the other samples analyzed, suggesting possible applications as a sensing material for both optical and electrochemical systems.
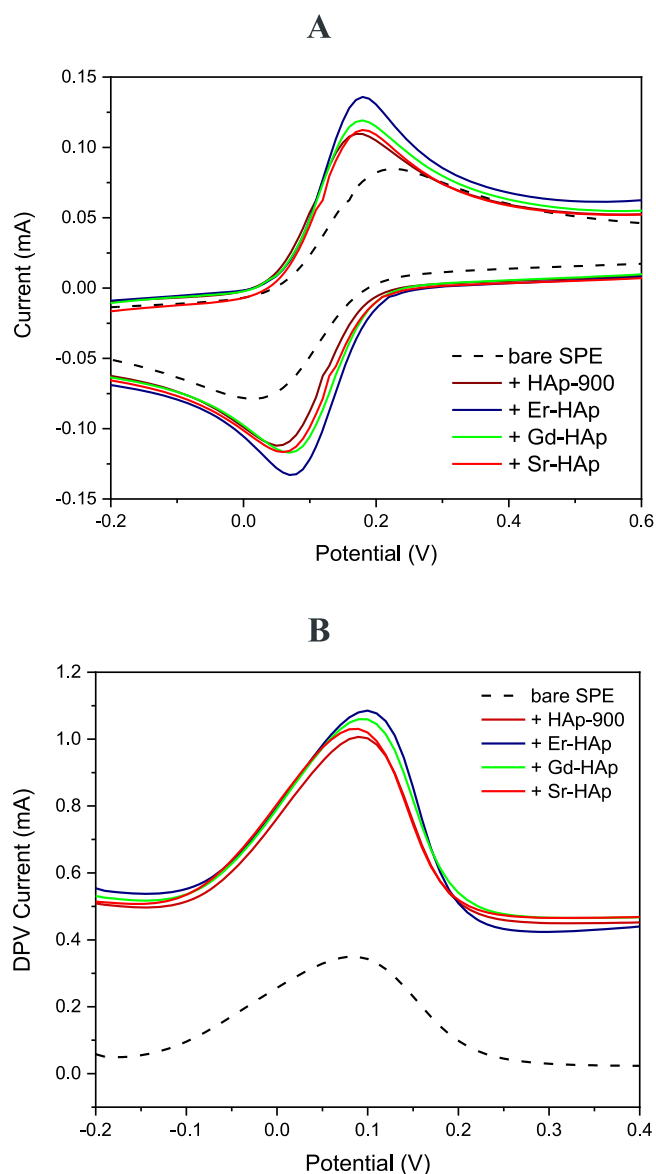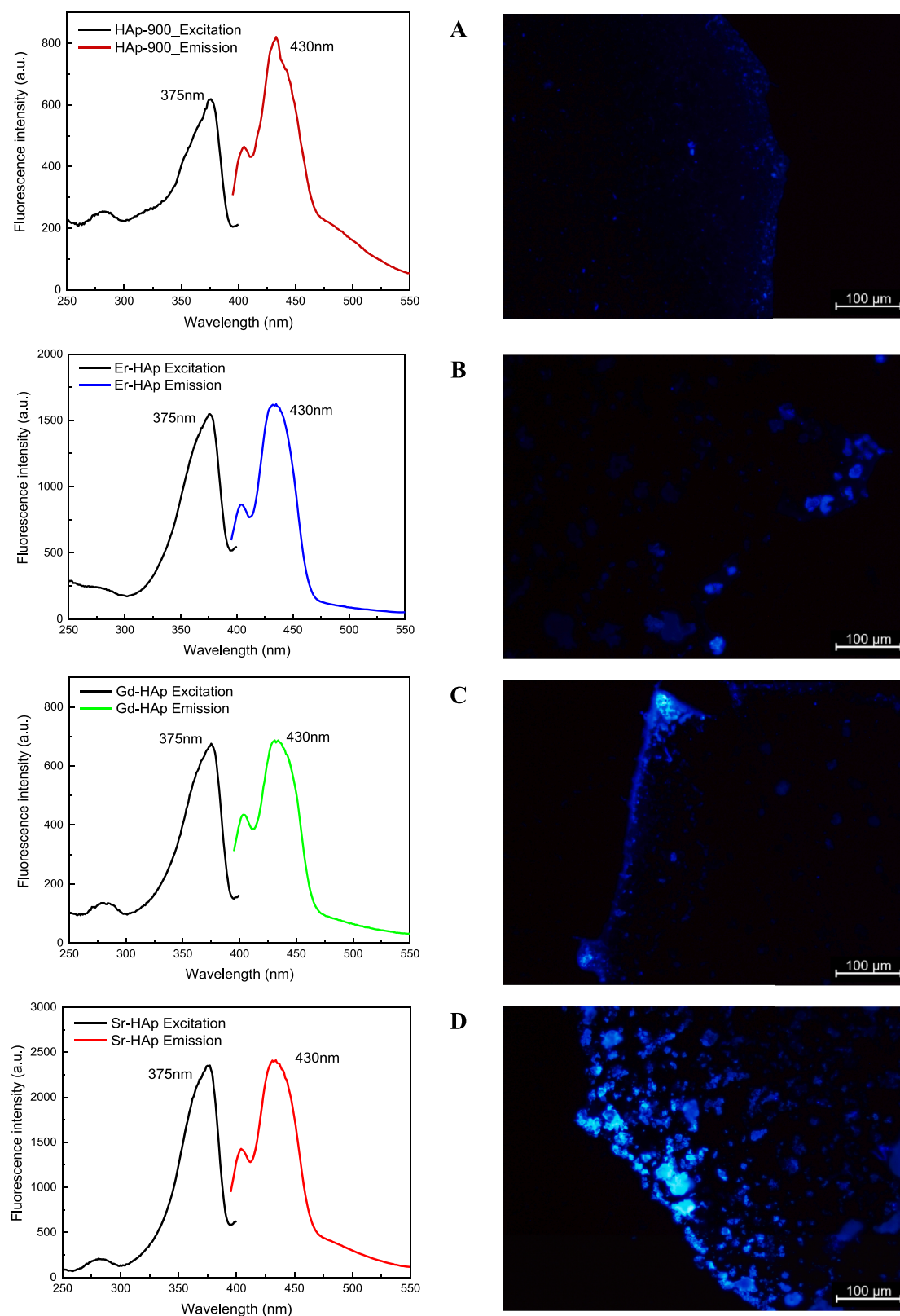
Fig. 11. Fluorescence spectra and fluorescence microscopy images of HAp samples: A) HAp-900, B) Er-HAp, C) Gd-HAp, and D) Sr-HAp. Signal acquisition window at 250–400 nm for the absorption spectrum and 400- 550 nm for the fluorescence emission spectrum (with Ex wavelength at 375 nm).

Funding

CRediT authorship contribution statement

Viviana Scognamiglio: Writing – review & editing, Writing – original draft, Validation, Supervision, Methodology, Investigation,

Formal analysis, Data curation, Conceptualization. **Valeria Nocerino:** Investigation, Formal analysis. **Bruno Miranda:** Investigation, Formal analysis. **Luca De Stefano:** Investigation, Formal analysis. **Emanuela Tempesta:** Investigation, Formal analysis. **Manuela Rossi:** Writing – review & editing, Investigation, Formal analysis. **Francesco Baldassarre:** Writing – review & editing, Investigation, Formal analysis. **Angela Altomare:** Writing – review & editing, Investigation, Formal analysis. **Francesco Capitelli:** Writing – review & editing, Writing – original draft, Visualization, Validation, Supervision, Investigation, Formal analysis, Data curation, Conceptualization.

Declaration of competing interest

The authors declare that they have no known competing financial interests or personal relationships that could have appeared to influence the work reported in this paper.

Acknowledgments

References

[1] M. Rossi, M.R. Ghiara, G. Chita, F. Capitelli, Crystal-chemical and structural characterization of fluorapatites in ejecta from somma-vesuvius volcanic complex, Am. Miner. 96 (2011) 1828–1837, https://doi.org/10.2138/am.2011.3803.

[2] F. Baldassarre, A. Altomare, N. Corriero, E. Mesto, M. Lacalamita, G. Bruno, A. Sacchetti, B. Dida, D. Karaj, G.Della Ventura, F. Capitelli, D. Siliqi, Crystal chemistry and luminescence properties of eu-doped polycrystalline hydroxyapatite synthesized by chemical precipitation at room temperature, cryst. 10 (2020) 250, https://doi.org/10.3390/cryst10040250.

[3] V. Paterlini, M. Bettinelli, R. Rizzi, A. El Khouri, M. Rossi, G.Della Ventura, F. Capitelli, Characterization and luminescence of Eu^{3+}- and Gd^{3+}-doped hydroxyapatite $Ca_{10}(PO_4)_6(OH)_2$, cryst. 10 (2020) 806, https://doi.org/10.3390/cryst10090806.

[4] M. Pasero, A.R. Kampf, C. Ferraris, I.V. Pekov, J. Rakovan, T.J. White, Nomenclature of the apatite supergroup minerals, Eur. J. Mineral. 22 (2010) 163–179, https://doi.org/10.1127/0935-1221/2010/0022-2022.

[5] P.M. Ihlen, H. Schiellerup, H. Gautneb, Ø. Skår, Characterization of apatite resources in Norway and their REE potential — A review, Ore Geology Rev. 58 (2014) 126–147, https://doi.org/10.1016/j.oregeorev.2013.11.003.

[6] V.F. Buchwald, Phosphate Minerals in Meteorites and Lunar Rocks, in: J.O. Nriagu, P.B. Moore (Eds.), Phosphate Minerals, Springer, Berlin, Heidelberg, 1984, https://doi.org/10.1007/978-3-642-61736-2_5.

[7] H. Fitzek, A. Zankel, M. Dienstleder, J. Rattenberger, H. Schröttner, F. Hofer, Correlating whole sample EDS and Raman mappings – A case study of a Chelyabinsk meteorite fragment, Micron 153 (2022) 103177, https://doi.org/10.1016/j.micron.2021.103177.

[8] B. Foley, M. Greiner, G. McGlynn, W.W. Schmahl, Anatomical variation of human bone bioapatite crystallography, cryst. 10 (2020) 859, https://doi.org/10.3390/cryst10100859.

[9] T. Kono, T. Sakae, H. Nakada, T. Kaneda, H. Okada, Confusion between carbonate apatite and biological apatite (Carbonated Hydroxyapatite) in bone and teeth, Minerals 12 (2022) 170, https://doi.org/10.3390/min12020170.

[10] N. Pretorius, A. Forrest, K.A. Walsh, Review of near infrared spectroscopic features of teeth, bone and artificial hydroxyapatite, J. Near Infrared Spectrosc. 31 (2023) 227–240, https://doi.org/10.1177/09670335231193117.

[11] V. Šromová, D. Sobola, P.A. Kaspar, Brief review of bone cell function and importance, Cells 12 (2023) 2576, https://doi.org/10.3390/cells12212576.

[12] [Updated 2023 May 17] J.L. Shaker, L. Deftos, et al., Calcium and phosphate homeostasis, in: KR Feingold, B Anawalt, MR Blackman, et al. (Eds.), Endotext [Internet], MDText.com, Inc., South DartmouthMA, 2000. Available from: https://www.ncbi.nlm.nih.gov/books/NBK279023/#.

[13] Y. Mu, Z. Du, L. Xiao, W. Gao, R. Crawford, Y. Xiao, The localized ionic microenvironment in bone modelling/remodelling: a potential guide for the design of biomaterials for bone tissue engineering, J. Funct. Biomater. 14 (2023) 56, https://doi.org/10.3390/jfb14020056.

[14] J. Engel, Enamel is the hardest biomaterial known. A Critical Survey of Biomineralization. SpringerBriefs in Applied Sciences and Technology, Springer, Cham, 2017, https://doi.org/10.1007/978-3-319-47711-4_5.

[15] M. Goldberg, A.B. Kulkarni, M. Young, A. Boskey, Dentin: structure, composition and mineralization, Front. Biosci. (Elite Ed) 3 (2011) 711–735, https://doi.org/10.2741/E281.

[16] Pu'ad Nor Mohd, Reazul Noh Haq, H. Abdullah, Hasan Idris, Maizlinda Te Chuan, Lee, Synthesis method of hydroxyapatite: a review, Mater. Today Proc. 29 (2020) 233–239, https://doi.org/10.1016/j.matpr.2020.05.536.

[17] Pilomeena Arokiasamy, Mohd Mustafa Al Bakri Abdullah, Shayfull Zamree Abd Rahim, Salmabanu Luhar, Andrei Victor Sandu, Noorina Hidayu Jamil, Marcin Nabiałek, Synthesis methods of hydroxyapatite from natural sources: a review, Ceram. Int. 48 (2022) 14959–14979, https://doi.org/10.1016/j.ceramint.2022.03.064.

[18] S. Adzila, I. Sopyan, M. Hamdi, Mechanochemical synthesis of hydroxyapatite nanopowder: effects of rotation speed and milling time on powder properties, Appl. Mech. Mater. 110 (2012) 3639–3644, https://doi.org/10.4028/www.scientific.net/AMM.110-116.3639.

[19] M. Toriyama, A. Ravaglioli, A. Krajewski, G. Celotti, A. Piancastelli, Synthesis of hydroxyapatite-based powders by mechano-chemical method and their sintering, J. Eur. Ceram. Soc. 16 (1996) 429–436, https://doi.org/10.1016/0955-2219(95)00123-9.

[20] N.V. M.V. Chaikina, N.V. Bulina, A.V. Ishchenko, I.Yu. Prosanov, Mechanochemical synthesis of hydroxyapatite and its modifications: composition, structure, and properties Russ. Phys. J. 56 (2014) 1176–1182, https://doi.org/10.1007/s11182-014-0159-0.

[21] S. Pramanik, A.K. Agarwal, K.N. Rai, A. Garg, Development of high strength hydroxyapatite by solid-state-sintering process, Ceram. Int. 33 (2007) 419–426, https://doi.org/10.1016/j.ceramint.2005.10.025.

[22] V.H. Arkin, M. Lakhera, I. Manjubala, U. Narendra Kumar, Solid state synthesis and characterization of calcium phosphate for biomedical application, Int. J. Chem. Tech. Res. 8 (2015) 264–267.

[23] M. Sadat-Shojai, M.T. Khorasani, E. Dinpanah-Khoshdargi, A. Jamshidi, Synthesis methods for nanosized hydroxyapatite with diverse structures, Acta Biomater. 9 (2013) 7591–7621, https://doi.org/10.1016/j.actbio.2013.04.012.

[24] J.S. Cho, Y.C. Kang, Nano-sized hydroxyapatite powders prepared by flame spray pyrolysis, J. Alloys Compd. 464 (2008) 282–287, https://doi.org/10.1016/j.jallcom.2007.09.092.

[25] A. Fihri, C. Len, R.S. Varma, A. Solhy, Hydroxyapatite: a review of syntheses, structure and applications in heterogeneous catalysis, Coord. Chem. Rev. 347 (2017) 48–76, https://doi.org/10.1016/j.ccr.2017.06.009.

[26] A. Yelten-Yilmaz, S. Yilmaz, Wet chemical precipitation synthesis of hydroxyapatite (HA) powders, Ceram. Int. 44 (2018) 9703–9710, https://doi.org/10.1016/j.ceramint.2018.02.201.

[27] N.V. Bulina, S.V. Makarova, S.G. Baev, A.A. Matvienko, K.B. Gerasimov, O. A. Logutenko, V.S. Bystrov, A study of thermal stability of hydroxyapatite, Minerals 11 (2021) 1310, https://doi.org/10.3390/min11121310.

[28] S. Graham, P.W. Brown, Reactions of octacalcium phosphate to form hydroxyapatite, J. Cryst. Growth 165 (1996) 106–115, https://doi.org/10.1016/0022-0248(95)00994-9.

[29] W.-J. Shih, Y.-F. Chen, M.-C. Wang, M.-H. Hon, Crystal growth and morphology of the nano-sized hydroxyapatite powders synthesized from $CaHPO_4·2H_2O$ and $CaCO_3$ by hydrolysis method, J. Cryst. Growth 270 (2004) 211–218, https://doi.org/10.1016/j.jcrysgro.2004.06.023.

[30] J.S. Earl, D.J. Wood, S.J. Milne, Hydrothermal synthesis of hydroxyapatite.. Published under licence by IOP Publishing, J. Phys.: Conf. Ser. 26 (2006) 268, https://doi.org/10.1088/1742-6596/26/1/064.

[31] D.-M. Liu, T. Troczynski, W.J. Tseng, Water-based sol–gel synthesis of hydroxyapatite: process development, Biomater 22 (2001) 1721–1730, https://doi.org/10.1016/S0142-9612(00)00332-X.

[32] M. Jevtic, M. Mitric, S. Skapin, B. Jancar, N. Ignjatovic, D. Uskokovic, Crystal structure of hydroxyapatite nanorods synthesized by sonochemical homogeneous precipitation, Cryst. Growth Des. 8 (2008) 2217–2222, https://doi.org/10.1021/cg7007304.

[33] Y. Han, X. Wang, S. Li, A simple route to prepare stable hydroxyapatite nanoparticles suspension, J. Nanopart. Res 11 (2009) 1235–1240, https://doi.org/10.1007/s11051-008-9507-8.

[34] M. Murray, J. Wang, C. Ponton, P. Marquis, An improvement in processing of hydroxyapatite ceramics, J. Mater. Sci. 30 (1995) 3061–3074, https://doi.org/10.1007/BF01209218.

[35] W. Zhou, M. Wang, W. Cheung, B. Guo, D. Jia, Synthesis of carbonated hydroxyapatite nanospheres through nanoemulsion, J. Mater. Sci: Mater. Med. 19 (2008) 103–110, https://doi.org/10.1007/s10856-007-3156-9.

[36] S.K. Saha, A. Banerjee, S. Banerjee, S. Bose, Synthesis of nanocrystalline hydroxyapatite using surfactant template systems: role of templates in controlling morphology, Mater. Sci. Eng. C 29 (2009) 2294–2301, https://doi.org/10.1016/j.msec.2009.05.019.

[37] Soo-Ling Bee, Z.A.A. Hamid, Hydroxyapatite derived from food industry bio-wastes: syntheses, properties and its potential multifunctional applications, Ceram. Int. 46 (2020) 17149–17175, https://doi.org/10.1016/j.ceramint.2020.04.103.

[38] L. Pastero, M. Bruno, D. Aquilano, About the genetic mechanisms of apatites: a survey on the methodological approaches, Minerals 7 (2017) 139, https://doi.org/10.3390/min7080139.

[39] R. Pérez-Solis, J.-J. Chen, B. Joseph, M.E. Mendoza, A. Moreno, Synthesis and characterization of a monoclinic crystalline phase of hydroxyapatite by synchrotron x-ray powder diffraction and piezoresponse force microscopy, cryst. 8 (2018) 458, https://doi.org/10.3390/cryst8120458.

[40] R. Canceliere, G. Rea, L. Micheli, P. Mantegazza, E.M. Bauer, A. El Khouri, E. Tempesta, A. Altomare, D. Capelli, F. Capitelli, Electrochemical and structural

characterization of lanthanum-doped hydroxyapatite: a promising material for sensing applications, Materials 16 (2023) 4522, https://doi.org/10.3390/ma16134522.

[41] I.D. Brown, D. Altermatt, Bond-valence parameters obtained from a systematic analysis of the inorganic crystal structure database, Acta Crystallogr. B Struct. Sci. 41 (1985) 244–247, https://doi.org/10.1107/S0108768185002063.

[42] F. Baldassarre, A. Altomare, E. Mesto, M. Lacalamita, B. Dida, A. Mele, E.M. Bauer, M. Puzone, E. Tempesta, D. Capelli, D. Siliqi, F. Capitelli, Structural characterization of low-sr-doped hydroxyapatite obtained by solid-state synthesis, cryst. 13 (2023) 117, https://doi.org/10.3390/cryst13010117.

[43] J. Angenault, J.C. Couturier, J.P. Souron, D. Siliqi, M. Quarton, The martensitic nature of the transition monoclinic ? Rhombohedral of $LiSn_2(PO_4)_3$, J. Mater. Sci. Lett. 11 (1992) 1705–1707, https://doi.org/10.1007/BF00736216.

[44] F.C. Hawthorn, Structure and chemistry of phosphate minerals, Mineral. Mag. 62 (1998) 141–164, https://doi.org/10.1180/002646198547512.

[45] F. Capitelli, M. Rossi, M. ElKhouri, M. Elaatmani, N. Corriero, A. Sodo, G. D. Ventura, Synthesis, structural model and vibrational spectroscopy of lutetium tricalcium phosphate $Ca_9Lu(PO_4)_7$, J. Rare Earths 36 (2018) 1162–1168, https://doi.org/10.1016/j.jre.2018.02.014.

[46] Inorganic Crystal Structure Database (ICSD) – Cambridge Structural Database (CSD), Cambridge Crystallographic Data Centre, 2024. UK, https://www.ccdc.cam.ac.uk/structures/ (accessed 30 july 2024).

[47] O. Ursini, E. Lilla, R. Montanari, The investigation on cationic exchange capacity of zeolites: the use as selective ion trappers in the electrokinetic soil technique, J. Hazard. Mater. 137 (2006) 1079–1088, https://doi.org/10.1016/j.jhazmat.2006.03.070.

[48] Tajammul Hussain M. Mysore, Arun Y. Patil, Chandrashekhar Hegde, M. A. Sudeept, Raman Kumar, Manzoore Elahi M. Soudagar, I.M.R. Fattah, Apatite insights: from synthesis to biomedical applications, Eur. Polym. J. 209 (2024) 112842, https://doi.org/10.1016/j.eurpolymj.2024.112842.

[49] I. Ielo, G. Calabrese, G. De Luca, S. Conoci, Recent advances in hydroxyapatite-based biocomposites for bone tissue regeneration in orthopedics, Int. J. Mol. Sci. 23 (2022) 9721, https://doi.org/10.3390/ijms23179721.

[50] S. Lara-Ochoa, W. Ortega-Lara, C.E. Guerrero-Beltrán, Hydroxyapatite nanoparticles in drug delivery: physicochemistry and applications, Pharmaceutics 13 (2021) 1642, https://doi.org/10.3390/pharmaceutics13101642.

[51] K. O'Hagan-Wong, J. Enax, F. Meyer, B. Ganss, The use of hydroxyapatite toothpaste to prevent dental caries, Odontology 110 (2022) 223–230, https://doi.org/10.1007/s10266-021-00675-4, 2022.

[52] C.G. Renda, T.M.d.O. Ruellas, J.O.D. Malafatti, C.S.S. Araújo, G.L.d. Silva, B.A. M. Figueira, S. Quaranta, E.C. Paris, A "Zero-Cost" adsorbing hydroxyapatite-based material from amazon fishery waste for water remediation and nutrient release for agriculture, Physchem 3 (2023) 34–60, https://doi.org/10.3390/physchem3010004.

[53] F. Capitelli, B. Dida, G.Della Ventura, F. Baldassarre, D. Capelli, G.S. Senesi, A. Mele, D. Siliqi, Functional nano-hydroxyapatite for applications in conservation of stony monuments of cultural heritage, Proc. AMIA Annu. Fall Symp. 62 (2020) 11, https://doi.org/10.3390/proceedings2020062011.

[54] S. Venkatesan, M.u. Hassan, H.J. Ryu, Adsorption and immobilization of radioactive ionic-corrosion-products using magnetic hydroxyapatite and cold-sintering for nuclear waste management applications, J. Nucl. Mater. 514 (2019) 40–49, https://doi.org/10.1016/j.jnucmat.2018.11.026.

[55] S. Pai, S.M. Kini, R. Selvaraj, A. Pugazhendhi, A review on the synthesis of hydroxyapatite, its composites and adsorptive removal of pollutants from wastewater, J. Water Process Eng. 38 (2020) 101574, https://doi.org/10.1016/j.jwpe.2020.101574.

[56] M. Ibrahim, M. Labaki, J.M. Giraudon, J.F. Lamonier, Hydroxyapatite, a multifunctional material for air, water and soil pollution control: a review, J. Hazard. Mater. 383 (2020) 121139, https://doi.org/10.1016/j.jhazmat.2019.121139.

[57] R. Verma, S.R. Mishra, V. Gadore, M. Ahmaruzzaman, Hydroxyapatite-based composites: excellent materials for environmental remediation and biomedical applications, Adv. Colloid Interface Sci. 315 (2023) 102890, https://doi.org/10.1016/j.cis.2023.102890.

[58] Balamurugan Senthil Kumar, Chiu-Wen Chen, Raja Nehru, Cheng-Di Dong, Electrocatalytic behavior of hydroxyapatite/graphene oxide nanocomposite-based sensor for electrochemical antioxidant monitoring of diphenylamine, Microchem. J. 195 (2023) 109504, https://doi.org/10.1016/j.microc.2023.109504.

[59] M. Tang, J. Shen, X. Xia, B. Jin, K. Chen, T. Zeng, A novel microbial induced synthesis of hydroxyapatite with highly efficient adsorption of uranyl(VI), Colloids Surf. A: Physicochem. Eng. Asp. 635 (2022) 128046, https://doi.org/10.1016/j.colsurfa.2021.128046.

[60] Yeni Wahyuni Hartati, Irkham Irkham, Salsha Zulqaidah, Ratu Shifa Syafira, Irwan Kurnia, Atiek Rostika Noviyanti, Seda Nur Topkaya. Recent advances in hydroxyapatite-based electrochemical biosensors: applications and future perspectives, Sens. Bio-Sens. Res. 38 (2022) 100542, https://doi.org/10.1016/j.sbsr.2022.100542.

[61] A. Curulli, Electrochemical biosensors in food safety: challenges and perspectives, Molecules 26 (2021) 2940, https://doi.org/10.3390/molecules26102940.

[62] Apurba Das, D. Pamu, A comprehensive review on electrical properties of hydroxyapatite based ceramic composites, Mater. Sci. Eng. C 101 (2019) 539–563, https://doi.org/10.1016/j.msec.2019.03.077.

[63] C. L. Khtaoui, M. Laghrouche, F. Fernane, C. Ahcène, High-sensitivity humidity sensor based on natural hydroxyapatite J. Mater. Sci.: Mater. in Electron. 32 (2021) 8668–8686, https://doi.org/10.1007/s10854-021-05538-w.

[64] G. Ramezani, I. Stiharu, T.G.M. van de Ven, V. Nerguizian, Advancement in biosensor technologies of 2D material integrated with cellulose-physical properties, Micromachines 30 (2023) 82, https://doi.org/10.3390/mi15010082.

[65] W. X. Mo, D. Zhang, K. Liu, X. Zhao, X. Li, W. Wang, Nano-hydroxyapatite composite scaffolds loaded with bioactive factors and drugs for bone tissue engineering Int. J. Mol. Sci. 24 (2023) 1291, https://doi.org/10.3390/ijms24021291.

[66] M. Jarcho, C.H. Bolen, M.B. Thomas, et al., Hydroxylapatite synthesis and characterization in dense polycrystalline form, J. Mater. Sci. 11 (1976) 2027–2035, https://doi.org/10.1007/BF02403350.

[67] A. Altomare, C. Cuocci, C. Giacovazzo, A. Moliterni, R. Rizzi, N. Corriero, A. Falcicchio, EXPO2013 : a kit of tools for phasing crystal structures from powder data, J. Appl. Crystallogr. 46 (2013) 1231–1235, https://doi.org/10.1107/S0021889813013113.

[68] A. Altomare, G. Campi, C. Cuocci, L. Eriksson, C. Giacovazzo, A. Moliterni, R. Rizzi, P.-E. Werner, Advances in powder diffraction pattern indexing: N-TREOR09, J. Appl. Crystallogr. 42 (2009) 768–775, https://doi.org/10.1107/S0021889809025503.

[69] A. Altomare, N. Corriero, C. Cuocci, A Falcicchio, A. Moliterni, R. Rizzi, QUALX2.0: a qualitative phase analysis software using the freely available database POW_COD, J. Appl. Crystallogr. 48 (2015) 598–603, https://doi.org/10.1107/S1600576715002319.

[70] PDF-2 ICDD, The Powder Diffraction File, International Center for Diffraction Data, Newton Square, PA, USA, 2003. Available online: https://www.icdd.com/pdf-2/.

[71] Dropsens, Spain, https://metrohm-dropsens.com, 2024 (accessed 30 july 2024).

[72] Palmsens, Netherlands https://www.palmsens.com, 2024, (accessed 30 july 2024).

[73] A. Altomare, R. Rizzi, M. Rossi, A. El Khouri, M. Elaatmani, V. Paterlini, G. Della Ventura, F. Capitelli, New $Ca_{2.90}(Me^{2+})_{0.10}(PO_4)_2$ β-tricalcium phosphates with Me^{2+} = Mn, Ni, Cu: synthesis, crystal-chemistry, and luminescence properties, cryst. 9 (2019) 288, https://doi.org/10.3390/cryst9060288.

[74] L.O. Ahmed, N. Bulut, L. Bañares, O. Kaygili, H. Kebiroglu, T. Ates, S. Koytepe, B. Ates, Exploring the electronic band structure, spectroscopic signatures, and structural properties of Er^{3+}-based hydroxyapatites co-doped with Ce^{3+} ions, Inorg. Chem. Comm. 155 (2023) 111067, https://doi.org/10.1016/j.inoche.2023.111067.

[75] B.K.S. Kumar, M. Jagannatham, B. Venkateswarlu, R. Dumpala, B.Ratna Sunil, Synthesis, characterization, and antimicrobial properties of strontium-substituted hydroxyapatite, J. Aust. Ceram. Soc. 57 (2021) 195–204, https://doi.org/10.1007/s41779-020-00525-6.

[76] D.O. Obada, K.A. Salami, A.N. Oyedeji, O.O. Fasanya, M.U. Suleiman, B.A. Ibisola, A.Y. Atta, D. Dodoo-Arhin, L.S. Kuburi, M. Dauda, E.T. Dauda, Solution combustion synthesis of strontium-doped hydroxyapatite: effect of sintering and low compaction pressure on the mechanical properties and physiological stability, Mater. Lett. 304 (2021) 130613, https://doi.org/10.1016/j.matlet.2021.130613.

[77] M. Lakrat, H. Jodati, M. El Miloud, Z. Evis, Synthesis and characterization of pure and Mg, Cu, Ag, and Sr doped calcium-deficient hydroxyapatite from brushite as precursor using the dissolution-precipitation method, Powder Technol. 413 (2023), https://doi.org/10.1016/j.powtec.2022.118026.

[78] M. Megha, Anjumol Joy, Gayathri Unnikrishnan, M. Haris, Jibu Thomas, Ayswaria Deepti, P.S. Baby Chakrapani, Elayaraja Kolanthai, Senthilkumar Muthuswamy, Structural and biological properties of novel Vanadium and Strontium co-doped HAp for tissue engineering applications, Ceram. Int. 49 (2023) 30156–30169, https://doi.org/10.1016/j.ceramint.2023.06.272.

[79] D. Chatelain, A. Denoirjean, V. Guipont, F. Rossignol, N. Tessier-Doyen, Influence of the thermal treatment of a hydroxyapatite powder on the characteristics of coatings deposited by cold gas spraying, Surf. Coat. Technol. 446 (2022) 128697, https://doi.org/10.1016/j.surfcoat.2022.128697.

[80] N. Méndez-Lozano, M. Apátiga-Castro, K.M. Soto, A. Manzano-Ramírez, M. Zamora-Antuñano, C. Gonzalez-Gutierrez, Effect of temperature on crystallite size of hydroxyapatite powders obtained by wet precipitation process, J. Saudi Chem. Soc. 26 (2022) 101513, https://doi.org/10.1016/j.jscs.2022.101513.

[81] A. Kurzyk, A. Szwed-Georgiou, J. Pagac, et al., Calcination and ion substitution improve physicochemical and biological properties of nanohydroxyapatite for bone tissue engineering applications, Sci. Rep. 13 (2023) 15384, https://doi.org/10.1038/s41598-023-42271-2.

[82] G. Mahmutoglu, A. Topsakal, E. Altan, et al., Effects of temperature and pH on the synthesis of nanohydroxyapatite powders by chemical precipitation, J. Aust. Ceram. Soc. 59 (2023) 1433–1441, https://doi.org/10.1007/s41779-023-00927-2.

[83] Morphologi G3, Malvern Panalytical, 2024. UK, https://www.malvernpanalytical.com/en/support/product-support/morphologi-range/morphologi-g3. accessed 30 july 2024.

[84] Thanigai Arul, Kumaravelu, Jayapalan Ramana Ramya, Subbaraya Narayana Kalkura, Impact of dopants on the electrical and optical properties of hydroxyapatite, Biomaterials. IntechOpen. Available at (2020), https://doi.org/10.5772/intechopen.93092.

[85] E. Landi, A. Tampieri, G. Celotti, S. Sprio, Densification behaviour and mechanisms of synthetic hydroxyapatites, J. Eur. Ceram. Soc. 20 (2000) 2377–2387, https://doi.org/10.1016/S0955-2219(00)00154-0.

[86] K. I. Grigoraviciute-Puroniene, Y. Tanaka, V. Vegelyte, Y. Nishimoto, K. Ishikawa, A. Kareiva, A novel synthetic approach to low-crystallinity calcium deficient hydroxyapatite Ceram. Int. 45 (2019) 15620–15623, https://doi.org/10.1016/j.ceramint.2019.05.072.

[87] V.V. Skorokhod, S.M. Solonin, V.A. Dubok, L.L. Kolomiets, T.V. Permyakova, A. V. Shinkaruk, Decomposition activation of hydroxyapatite in contact with

tricalcium phosphate, Powder Metall. Metal. Ceram. 49 (2010) 324–329, https://doi.org/10.1007/s11106-010-9239-z.

[88] F. Capitelli, B. El Bali, R. Essehli, M. Lachkar, I. da Silva, New hybrid diphosphates Ln$_2$(NH$_2$(CH$_2$)$_2$NH$_2$)(HP$_2$O$_7$)$_2$·4H$_2$O (Ln = Eu, Tb, Er): synthesis, single crystal and powder X-ray crystal structure, Z. Kristallogr. 221 (2006) 788–794, https://doi.org/10.1524/zkri.2006.221.12.788.

[89] B. El Bali, F. Capitelli, A.T. Alaoui, M. Lachkar, I. da Silva, A. Alvarez-Larena, J. F. Piniella, New thallium diphosphates Tl$_2$Me(H$_2$P$_2$O$_7$)$_2$·2H$_2$O, Me = Mg, Mn, Co, Ni and Zn. Synthesis, single crystal X-ray structures and powder X-ray structure of the Mg phase, Z. Kristallogr. 223 (2008) 448–455, https://doi.org/10.1524/zkri.2008.0047.

[90] B.O. Fowler, Infrared studies of apatites. I. Vibrational assignments for calcium, strontium, and barium hydroxyapatites utilizing isotopic substitution, Inorg. Chem. 13 (1974) 194–207, https://doi.org/10.1021/ic50131a039.

[91] W. Jastrzębski, M. Sitarz, M. Rokita, K. Bułat, Infrared spectroscopy of different phosphates structures, Spectrochim. Acta Part A Mol. Biomol. Spectrosc. 79 (2011) 722–727, https://doi.org/10.1016/j.saa.2010.08.044.

[92] A. El Khouri, A. Zegzouti, M. Elaatmani, F. Capitelli, Bismuth-substituted hydroxyapatite ceramics synthesis: morphological, structural, vibrational and dielectric properties, Inorg. Chem. Commun. 110 (2019) 107568, https://doi.org/10.1016/j.inoche.2019.107568.

[93] N.V. Bulina, M.V. Chaikina, I.Y. Prosanov, Mechanochemical synthesis of sr-substituted hydroxyapatite, Inorg. Mater. 54 (2018) 820–825, https://doi.org/10.1134/S0020168518080034.

[94] M. Markovic, B.O. Fowler, M.S. Tung, Preparation and comprehensive characterization of a calcium hydroxyapatite reference material, J. Res. Natl. Inst. Stand. Technol. 109 (2004) 553, https://doi.org/10.6028/jres.109.042.